

See discussions, stats, and author profiles for this publication at: <https://www.researchgate.net/publication/298898142>

Wake analysis of aerodynamic components for the glide envelope of a jackdaw (*Corvus monedula*)

Article in *Journal of Experimental Biology* · March 2016

DOI: 10.1242/jeb.132480

CITATIONS

21

READS

694

3 authors, including:



Marco Klein Heerenbrink
University of Oxford

11 PUBLICATIONS 118 CITATIONS

[SEE PROFILE](#)



Anders Hedenström
Lund University

256 PUBLICATIONS 11,183 CITATIONS

[SEE PROFILE](#)

Some of the authors of this publication are also working on these related projects:



Quantifying aerodynamic performance of avian flight through wake analyses [View project](#)



Between- and within-individual variation in the annual movement of long-distance migrants [View project](#)

Wake analysis of aerodynamic components for the glide envelope of a jackdaw (*Corvus monedula*)

Marco KleinHeerenbrink*, Kajsa Warfvinge, Anders Hedenström*

Department of Biology, Lund University, SE-223 62 Lund, Sweden

*Authors for correspondence: Marco.Klein_Heerenbrink@biol.lu.se,
Anders.Hedenstrom@biol.lu.se

Abstract

Gliding flight is a relatively inexpensive mode of flight used by many larger bird species, where potential energy is used to cover the cost of aerodynamic drag. Birds have great flexibility in their flight configuration, allowing them to control their flight speed and glide angle. However, relatively little is known about how this flexibility affects aerodynamic drag.

We measured the wake of a jackdaw (*Corvus monedula*) gliding in a wind tunnel, and computed the components of aerodynamic drag from the wake. We found that induced drag was mainly affected by wingspan, but also that the use of the tail has a negative influence on span efficiency. Contrary to previous work, we found no support for the separated primaries being used in controlling the induced drag. Profile drag was of similar magnitude to that reported in other studies, and our results suggest that profile drag is affected by variation in wing shape. For a folded tail the body drag coefficient had a value of 0.2, rising to above 0.4 with the tail fully spread, which we conclude is due to tail profile drag.

Key words

Gliding flight, Biomechanics, Aerodynamics, Jackdaw (*Corvus monedula*), Particle Image Velocimetry (PIV), wind tunnel

Introduction

Gliding flight in birds is a relatively inexpensive mode of flying, at least in terms of instantaneous power required from the flight muscles (Baudinette and Schmidt-Nielsen, 1974). A bird only has to spend energy on keeping the wings spread. The cost of transport is covered by converting potential energy (altitude) into aerodynamic work. During soaring, potential energy is replenished by extracting energy from the environment, for example from the rising air in thermals (thermal soaring) or the wind shear gradient over the oceans (dynamic soaring). In the absence of external energy sources, a bird will need to use muscle power to gain altitude. Either way, gliding birds have a good reason to minimize aerodynamic drag. However, one can also think of circumstances in which it is beneficial to rapidly dissipate energy, for example during descent before landing. To accomplish this, birds can modify their flight configuration. The glide performance of birds has been studied in numerous previous works using tiltable wind tunnels (Henningsson and Hedenström, 2011; Pennycuick, 1968; Rosén and Hedenström, 2001; Tucker, 1987; Tucker and Heine, 1990; Tucker and Parrott, 1970) or using field observations (Eder et al., 2015; Pennycuick, 1971). However, it has always been difficult to measure the different components of drag. One strategy has been to mount body parts on a balance (Lentink et al., 2007; Pennycuick, 1968; Pennycuick et al., 1988; Tucker, 1990), however, it is not trivial to match the degree of flexibility in posture of a bird. There have been few attempts with wake pressure surveys behind the wings of living birds (Pennycuick et al., 1992), but this method only samples a small part of the wing at the time. Due to advances in technology we can now measure the entire wake of a bird in one instance, compute the different components of drag and relate them to adjustments in the bird's flight configuration.

In steady gliding flight the weight (W) of the bird is balanced by the aerodynamic force (Fig. 1A). By definition this force is decomposed into a lift component perpendicular to the flight path

$$L = W \cos \gamma, \quad (1)$$

and a drag component in the direction along the flight path

$$D = W \sin \gamma, \quad (2)$$

where γ is the angle between the flight path and the horizontal plane (see Fig. 1B). Using a tiltable wind tunnel (Pennycuick, 1968; Rosén and Hedenström, 2001) or by measuring the glide path (in relation to wind currents) in wild birds (Eder et al., 2015; Pennycuick, 1971) these equations can be used to determine the total drag experienced by a bird. Drag can be decomposed into three main sources. Lift induced drag (D_{ind}) is the cost of producing lift using wings. From the theory of flight mechanics we know this component behaves as

$$D_{\text{ind}} = \frac{L^2}{q\pi eb_w^2}, \quad (3)$$

where L is the lift force, $q = \frac{1}{2}\rho U^2$ is the dynamic pressure, itself a function of density ρ and airspeed U , b_w is the wingspan and e is the span efficiency factor (alternatively found in literature as its reciprocal $k_{\text{ind}} = 1/e$). The latter factor is an indicator of how efficiently lift is produced compared to an elliptically loaded planar wing of span b . From equation (3) it can be expected that a bird can increase induced drag by flexing its wings. We will refer to the inflight wingspan as b'_w and the related span efficiency $e' = e/\beta^2$, using $\beta = b'_w/b_w$ as ratio between inflight span and maximum span. The shape-specific span efficiency e' depends on the load distribution along the span of the wing, where $e' = 1$ is the reference of an elliptically loaded planar wing. This factor can be influenced by non-planar features, e.g. spanwise camber (Cone, 1962), vertical separation of the outer primaries (Berens,

2008; Tucker, 1993), and in case of a loaded tail, the vertical gap between the tail and main wing (Thomas, 1996).

Another component of drag is the wing profile drag, which describes more local interaction between the airflow and the wing surface. This component is commonly expressed as

$$D_{\text{pro}} = qC_{D_{\text{pro}}}S_w, \quad (4)$$

where S_w is the wing area and $C_{D_{\text{pro}}}$ is the profile drag coefficient. Equation (4) suggests that birds can reduce this component of drag by flexing their wings, which combined with the span dependency of induced drag leads to an optimal span model (Tucker, 1987). With $\zeta = S'_w/S_w$, the coefficient $C'_{D_{\text{pro}}} = C_{D_{\text{pro}}}/\zeta$ represents the shape-specific profile drag coefficient, which may vary due to pressure distribution and the state of the boundary layer across the exposed area of the shape. For a typical aerofoil the profile drag coefficient varies with lift coefficient following

$$C'_{D_{\text{pro}}} = C_{D_0} + k_{\text{pro}} \left(C'_L - C'_{L_{D_{\text{pro}}, \text{min}}} \right)^2, \quad (4)$$

or $C'_{D_{\text{pro}}} = c_0 + c_1 C'_L + c_2 C'^2_L$, where $C'_L = L/qS'_w$ is the shape-specific lift coefficient (Tucker, 1987).

The last component is the body drag, which describes the local interaction between the airflow and the body (and appendages). This component can be expressed as

$$D_{\text{body}} = qC_{D_b}S_b, \quad (5)$$

where the reference area is now the body frontal area S_b and the body drag coefficient C_{D_b} describes the characteristics of the body shape. For body frontal area we use the allometric relation $S_b = 0.0129m^{0.614} = 5.0 \times 10^{-3} \text{ m}^2$ from (Rosén et al., 2003), which corresponds to a disc radius of about 4 cm. The body drag coefficient may vary with Reynolds number $Re = Ul/\nu$ (Hedenström and Liechti, 2001), body angle

(Hoerner, 1965), extension of the legs (Pennycuick, 1968) and tail deployment (Thomas, 1996).

With the emergence of Particle Image Velocimetry (PIV) it is now possible to measure the flow field in the wake behind a flying bird (Spedding et al., 2003). This wake contains information about the forces that the bird applied to the air as it passed through it (Henningsson and Hedenström, 2011; Pennycuick et al., 1992; Spedding, 1987). With the current state of technology we can differentiate between the different drag sources in a freely gliding bird, measuring profile drag and body drag as the streamwise velocity deficit and induced drag as the cross-flow kinetic energy. We can then relate the variation in these forces with the variation in posture, and hence work out how birds control their flight. In this paper we present such measurements from the wake of a jackdaw (*Corvus monedula*) gliding in a tiltable wind tunnel. We investigate the hypotheses that (i) span efficiency increases with spanwise camber, primary separation and by use of the tail; (ii) profile drag coefficient is controlled by wing shape; (iii) body drag coefficient is increased by body angle and the use of the tail.

Materials and methods

The methods used in the experiments are largely similar to those described in (Rosén and Hedenström, 2001), with the addition of a Trefftz-plane flow velocity measurement using a stereo Particle Image Velocimetry (PIV) system and a stereo camera setup for three dimensional reconstruction of posture.

Experimental setup

For the experiments we used the low-turbulence tiltable wind tunnel at the Department of Biology, Lund University, Sweden. Details of the tunnel are described in (Pennycuik et al., 1997). The test section is 1.20 m wide, 1.08 m high and the closed section is approximately 1.2 m long. Downstream of this section is an approximately 0.5 m long gap that allows easy access to the bird and provides room for positioning PIV cameras outside of the flow (Fig. 1B).

The velocity field in a plane perpendicular to the free stream flow in the wake behind the bird was measured using a PIV system recording 640 frame-pairs per second. Two LaVision Imager pro HS 4M high-speed cameras 2016x2016 px (LaVision GmbH, Goettingen, Germany) in stereo configuration were aimed at the left wing tip vortex and an additional two cameras were aimed at the inner wing and body wake region. The combined resolved flow field had a width of 0.45 m and a height of 0.35 m. A 527 nm diode pumped LDY304PIV laser (Litron Lasers Ltd, Rugby, England) was used to illuminate particles ($\sim 1\text{ }\mu\text{m}$) in a sheet, approximately 3 mm thick in the streamwise direction, aligned with the plane of focus of the cameras.

The posture of the bird was captured using two LaVision HighSpeedStar3 high-speed cameras 1024x1024 px in stereo configuration looking down on the bird from the top of the test section (Fig. 1B). The cameras were calibrated with a moving checkerboard

pattern using routines from the Matlab Computer Vision Toolbox (The Mathworks, Inc. Natick, MA, USA).

Study species

Gliding flight is frequently used by relatively larger birds (Hedenström, 1993). Jackdaws are among the smaller species that extensively use gliding flight in the wild, which makes them suitable for this experiment considering the size limitations of the test section of the wind tunnel. A young jackdaw was taken from a nest near Revingehed, Skåne, Sweden, around the time of fledging (June 11, 2013). The bird was kept in an indoor aviary measuring 1.5 m × 1.5 m × 2 m. Food (primarily dried cat food and oats) and water (drinking and bathing) were made available at libitum. Food and bathing water were removed one hour before training or experiments, in order to keep the bird motivated and to prevent it from getting soaked. The bird was trained, using positive reinforcement (audible cues followed by a food reward), to return to the experimenter's hand, to stand on a weighing scale, and to keep position when flying in the wind tunnel. It was introduced to the wind tunnel one week after capture. The bird reached its final weight within two weeks of capture. Due to technical issues the first usable experiments were recorded on August 20, 2013.

Following the procedure described by Pennycuick (Pennycuick, 2008), maximum wingspan was measured from the bird in the hand as $b_w=0.67$ m and wing area was determined from a tracing as $S_w=0.0652$ m². During the experiments the mass of the bird was measured before and after each session, ranging from 0.211 kg to 0.221 kg averaging at 0.215 kg.

Experiments were carried out under permission M 33-13 from the Malmö-Lund animal ethics committee.

Posture reconstruction

At each tilt angle (except at 5.0 degrees) a calibration was computed following the stereo calibration tool of the Matlab Computer Vision Toolbox. The cameras were positioned above the bird, where camera one was approximately perpendicular to the streamwise-spanwise plane. Reconstructed points had an estimated reconstruction error in the plane of camera one of less than 0.5 mm and about 2 mm in the out-of-plane direction. For the glide angle of 5.0° no calibration was available, so the calibration at 5.5°, which was most similar, was used. Due to the rotating of the wind tunnel, camera two had moved a small amount between 5.0° and 5.5°. As a result the estimated reconstruction errors at the glide angle of 5.0° were an order of magnitude larger: ~1 mm in plane and 12 mm out of plane. In each view several key points were digitized (see supplementary material Fig. S2): the tip of the primary feathers (1-10), the tip of the secondary feathers (11-18), tertials contour (19-20), tip of the rectrices (tail feathers) (21-26), body centre line (27-28), the shoulder joint (29) and the wrist joint (30). Points 19, 20 and 27 to 30 are not physical marks consistent over all sequences. Instead variable consistent marks are identified within each sequence. Point 27 (neck) is located at the collar at the transition between fine feathers on the head and the larger body contour feathers. The feathers on the head meet at the centre line of the head, resulting in temporary natural markers that can be identified in both views throughout several frames. Point 28 (rump) is horizontally aligned between the two central rectrices, and its streamwise location was determined similar to point 27. The reconstructed points were mirrored in the vertical plane through the body centre line 27-28, and the result was visually checked for errors. Wingspan (b'_w) was determined from the maximum distances between any primary feather point to its respective mirrored point. Wing area (S'_w) was computed as the enclosed area

between points 1 to 18, 29, and 30 and their mirrored points. Tail span (b_t') was determined analogous to wingspan using the rectrix points instead. For the tail area (S_t') an additional point was required, which was positioned 1/3 the distance from the rump to neck (approximately extension of R6 to the body centre line). The body angle was determined from the x (streamwise) and z (vertical) coordinates of points 27 and 28. Spanwise camber (η_w) was calculated as the height of a circular arc segment through the y and z coordinates of points 1-6 and 11-16 and their mirrored points. The coordinates were first normalized to the in-flight wingspan and centred. Through non-linear least squares a circle with radius R and vertical centre z_c was fitted to these points: $z(y) = \sqrt{R^2 - y^2} + z_c$. The spanwise camber was then calculated as the height of the segment:

$$\eta_w = R - \sqrt{R^2 - \frac{1}{4}}. \quad (7)$$

Note that η_b indicates the height as a fraction of the in-flight wingspan. Only fitted curves with $r^2 > 0.9$ were used, as lower quality fitted curves differed considerably from the reconstructed wing shape. Primary separation was determined as the distance (still in the normalized and centred coordinates) of primary 8 away from the arc segment, i.e. as

$$\eta_p = \sqrt{y_p^2 + (z_p + z_c)^2} - R. \quad (8)$$

Vertical tail gap was determined from the vertical difference between the mean location of points 11-18 (secondaries) and that of points 21-26 (rectrices).

Wake analysis

The wake velocity fields were computed in LaVision Davis 8.1 (LaVision GmbH, Goettingen, Germany) using a weighted sliding sum of correlation routine (± 2 frames; multipass 64×64 px, 50% overlap $2 \times$ to 16×16 px, 50% overlap; delete correlation

value < 0.6 ; $1\times$ strongly remove ($>2\times\text{rms}$), iteratively insert ($<3\times\text{rms}$)). This routine was chosen to compensate the low correlations due to particle loss (due to the largest particle displacement occurring in the smallest dimension of the laser sheet). The raw vector fields were then further processed in Matlab (The Mathworks, Inc. Natick, MA, USA). At each speed each view showed a small but distinct false pattern in the background flow in the streamwise direction, most likely due to the relatively high velocity perpendicular to the measurement plane. This pattern was removed by constructing an average second order surface polynomial, for each combination of speed and glide angle, that was subtracted from the measured flow and replaced with a uniform streamwise velocity based on the mean velocity from the polynomial. Then the two views were merged using weighted averaging favouring vectors with lower temporal signal noise. From the merged velocity field sequence segments of 40 to 60 frames (63–94 ms) were selected, during which the wake did not notably displace or change shape. For these segments the time average velocity field $\bar{\mathbf{u}}$ and the root-mean-squared time fluctuations \mathbf{u}' were computed. As only the wake from the left wing and the body wake were captured a symmetry-plane was defined manually, depending on the available information in the wake to best estimate the location of the right wing tip vortex (see Fig. 2).

Aerodynamic forces on an object immersed in a flow can be computed using a control volume approach (Noca et al., 1999; van Oudheusden et al., 2006). Using such an approach, lift was computed using the wake velocity field equation

$$L = \rho \iint y \bar{u} \bar{\omega} dS + \rho \iint y \left\{ \bar{w} \frac{\partial \bar{u}}{\partial y} + \bar{v} \frac{\partial \bar{u}}{\partial z} \right\} dS, \quad (9)$$

where $\bar{\omega} = (\nabla \times \bar{\mathbf{u}}) \cdot \mathbf{i}$ (van Dam et al., 1993). Induced drag was computed as

$$D_{\text{ind}} = \frac{1}{2} \rho \iint \psi \bar{\omega} dS + \frac{1}{2} \rho \iint (v'^2 + w'^2) dS, \quad (10)$$

where ψ is the cross-flow stream function solved from $\nabla^2\psi = -\bar{\omega}$ with Dirichlet boundary conditions $\psi = 0$ on the wind tunnel walls (using the function `adaptmesh()` from the Matlab partial Differential Equation toolbox). Body drag was computed as

$$D_{\text{bod}} = \rho \iint_{\text{body}} (\bar{u}(U_{\infty} - \bar{u}))dS - \rho \iint_{\text{body}} u'^2 dS, \quad (11)$$

where the body region was defined manually for every wake based on the pattern of the streamwise velocity perturbation (see Fig. 2). Profile drag of the tail is included in this body drag term, even when the tail was widely spread. Wing profile drag was computed using

$$D_{\text{pro}} = \iint_{\text{pro}} (\bar{u}(U_{\infty} - \bar{u}))dS - \rho \iint_{\text{pro}} u'^2 dS, \quad (12)$$

where the profile drag region was manually masked to include only the velocity deficit due to the wings and to minimize the influence of noise outside of the actual wake (see Fig. 2). Equations (10) to (12) are derived through a control volume approach, e.g. (Giles and Cummings, 1999; van Dam, 1999), where equation (10) is the result in case of only induced drag, while equations (11) and (12) result in case of only profile drag or body drag respectively.

Equation (10) only takes into account the affected airstream within the boundaries of the wind tunnel walls. For a bird the size of the jackdaw this results in a reduction in induced drag of 10%-15% compared to what the same distribution of vorticity would produce in an unbounded flow. Shape-specific span efficiency e' was corrected for this wall effect by

$$e' = \left(\frac{\beta^2}{e} + \sigma \right)^{-1}, \quad (13)$$

where σ depends on the ratio of wingspan to wind tunnel width and the vertical position in the tunnel. Details on this correction can be found in the supplementary

material (Fig S1). Effects of wake blockage and solid blockage were found to be negligible: $(\Delta u/U_\infty)_{wb} \ll 1\%$ (Barlow et al., 1999 p. 374).

Weight support and effective glide angle

For perfect steady gliding flight the total aerodynamic force should balance the weight of the bird. In that case the weight support $\sqrt{L^2 + D^2}/W = 1$. If the measured values deviate from unity, this could indicate that something is wrong with the measurement or that the bird is not perfectly balanced or a combination of both. From our processed dataset we discarded measurements that deviated more than 20% from proper weight support. The remaining dataset ($N = 389$) had an average weight support of 1.04 with a standard deviation of 0.07. Fig. 3A shows the weight support averaged per combination of glide angle and speed.

The drag component is an order of magnitude smaller than the weight. The required drag for steady gliding flight is $D = W \sin \gamma$. The measured drag increased with decreasing glide angles from an average of 1.08 at 6° to 1.28 times the required drag at 4.5° (see also Fig. 3B). This trend can be explained simply by considering that at the shallowest glide angle the required drag matches the minimum drag the bird can produce. Any variation will then increase the average measured drag above that required for a steady glide. This is visualized in Fig. 3C. The bird in practice seems to experiences the same variation of drag at the instance of measurement irrespective of the prescribed glide angle. Any measurements should be only weakly related with the wind tunnel angle, due to on one hand the bird's intention to glide steadily and on the other hand the degree of unsteady aerodynamics involved. We therefore constructed an alternative (quasi-steady) glide angle based on the measured combinations of lift and drag. For visualization purposes we grouped these to the closest half-degree. This

left the angles 5.0°, 5.5°, 6.0° and 6.5°+, the latter also containing all angles larger than 6.5°. Regressions were performed on the complete dataset.

Statistics and data availability

In total 414 wakes were analysed, of which 389 were within 20% of weight support. For 118 of these wakes the posture was analysed. All regressions were performed using the `fitlm()` function of the Matlab Statistics Toolbox (The Mathworks, Inc. Natick, MA, USA), with response and predictor variables as continuous variables. Summary tables for regressions between aerodynamic components and measures of posture and the complete dataset are made available as the supplementary material.

Results

Wake topology

Fig. 2 shows a typical wake as captured behind the gliding jackdaw. We measured the wake at a distance of approximately one half to one full wingspan behind the bird. The vorticity that is shed from the wings has had little time to roll-up into the tip vortices, so that we can still see regions of vorticity distributed along the span. In most conditions the tail is contributing some positive lift, so that we can also identify a vorticity distribution coming from the tail. Profile drag causes a thin region of decelerated flow leaving the wing. When the tail is spread, a similar region of decelerated flow can be identified for the tail, though only where the tail extends beyond the wake of the body. Behind the body a wider region of decelerated flow is visible. The deceleration in this region is much more substantial than for the wake of the wing. The body region often also contains four patches of vorticity organized as a quadrupole, where the top pair is separated from the lower pair by the tail. The lower pair has the same sign as the tail, i.e. reflecting positive lift, and often merges with tail vorticity. The top pair rotates in opposite sense. Due to the minimal distance from the spanwise centre, these vortices will not actually contribute significantly to the lift, however, their kinetic energy contributes to the measure of the induced drag.

Posture

Wingspan decreases substantially with speed from just over 90% of the maximum wingspan at the lowest speeds to about 75% at the higher speeds. However, we find no significant relationship with glide angle ($p_U < 10^{-31}$, $p_\gamma = 0.53$, $N = 118$, $r^2 = 0.68$ [notation p_U and p_γ indicating the p-value for the correlation with U and γ respectively]). Wing area is strongly linked to wingspan, so that wing area shows a

very similar pattern (Fig. 4B). In fact, the area ratio $\zeta = S'_w/S_w$ is almost linearly proportional to the span ratio $\beta = b'_w/b_w$ as shown in Fig. 4C. A linear regression, $\zeta = c_0 + c_1\beta$, gives $c_0 = -0.33 \pm 0.04$ and $c_1 = 1.44 \pm 0.04$ (mean \pm s.e.m., $N = 118$).

Tail span varied from 28% of the maximum wingspan at the lowest speed to 7% at the highest speed (Fig. 5A). Here we do find a significant positive relationship with glide angle ($p_U < 10^{-49}$, $p_\gamma < 0.001$, $N = 116$, $r^2 = 0.86$). As the tail of a jackdaw has a simple fan shape, its area follows the trend of the tail span (Fig. 5B).

Body angle was measured based on two soft markers on the bird's body, and the camera setup is most sensitive to errors in the vertical direction, so these body angle measurements should be interpreted with caution. However, body drag is likely to be a function of body angle and therefore it is an important parameter to consider. For the equivalent glide angles of 5.0° and 5.5° a decreasing trend is observed, going from 15° to about 7.0° (Fig. 6). The decrease is less apparent for the steeper angles of 6.0° and above. A linear model finds a negative relation with speed, but none with glide angle ($p_U = 0.002$, $p_\gamma = 0.44$, $N = 118$, $r^2 = 0.09$).

More subtle measures of posture include the non-planar features of the wing, which have been suggested as adaptations to minimize induced drag. The most typical for gliding jackdaws is the spanwise camber, where the outer wing is lowered below the wing root. This shape can be approximated as a circular arc segment, of which the span specific height η_w is shown in Fig. 7A. There does not seem to be a clear relation between spanwise camber and glide angle, but there is some tendency for it to increase with speed ($p_U < 10^{-5}$, $p_\gamma = 0.35$, $N = 96$, $r^2 = 0.21$). Separation of the outer primaries, η_p , also increases slightly with speed, as shown in Fig. 7B. Below 10 m s^{-1} the separation is more pronounced for the higher drag cases ($p_U <$

$10^{-5}, p_{\gamma} < 0.007, N = 71, r^2 = 0.32$). As shown in Fig. 7C the tail gap η_t varies non-linearly with speed. Below 9 m s^{-1} tail gap is relatively constant with speed and glide angle, averaging at 0.054 ± 0.002 , ($p_0 < 10^{-36}, N = 59$). Above 9 m s^{-1} η_t varies both with speed and glide angle, where tail gap is reduced at increasing speed, and a larger tail gap is related to increased total drag ($p_U < 10^{-4}, p_{\gamma} = 0.003, N=57$).

Components of drag

Span efficiency decreased with flight speed from around 1 to 0.7 (Fig. 8A), and it was generally lower for higher total drag ($p_U < 10^{-51}, p_{\gamma} < 10^{-7}, N = 389, r^2 = 0.51$). This corresponds to a large extent with the observed span reduction (Fig. 4A). If we remove the effect of wingspan and look at the shape-specific span efficiency e' , most of the variation has disappeared (Fig. 8B), with all values being relatively close to 1. With increasing speed there is a weak increase in e' , while there is a strong relation between decreased span efficiency and higher total drag ($p_U = 0.008, p_{\gamma} < 10^{-5}, N = 118, r^2 = 0.21$).

Shape-specific span efficiency can be influenced by non-planar features of the lifting surfaces: spanwise camber η_w , primary separation η_p , tail span β_t/β and vertical tail gap η_t . In a linear model including all four variables only tail span and tail gap have significant effects ($p_{\eta_w} = 0.31, p_{\eta_p} = 0.13, p_{\beta_t} = 0.048, p_{\eta_t} < 0.001, N = 94$), where notably an increase of tail gap of $0.01b'_w$ corresponds to a decrease in span efficiency of about 1-2% (see also Table S1). Despite the much lower confidence, spanwise camber, primary separation and tail span are attributed positive contribution to span efficiency.

The profile drag coefficient (Fig. 9A) decreased slightly with flight speed and was lower for smaller glide angles ($p_U < 10^{-4}, p_{\gamma} < 10^{-25}, N=387, r^2 = 0.26$). Taking

into account the in-flight wing area reduces the dependency on speed (Fig. 9B), but otherwise the effect is marginal. Fig. 9C shows the profile drag coefficient as a function of lift coefficient. Performing a linear regression $C'_{D_{\text{pro}}} = c_0 + c_1 C'_L + c_2 C'^2_L$ (equation (4)) on the data we find $k_{\text{pro}} = 0.030$, $C'_{L_{D_{\text{pro,min}}}} = 0.77$ and $C_{D_{\text{pro,min}}} = 0.019$ (using $C'_{D_{\text{pro,min}}} = c_0 - c_1^2/4c_2$ and $C'_{L_{D_{\text{pro,min}}}} = -\frac{c_1}{2c_2}$; see also Table S2). When we include parameters of wing shape, η_w and η_p , to the above regression model, we find that spanwise camber η_w may be affecting both c_0 ($p_{\eta_w} = 0.004$) and c_1 ($p_{\eta_w|C_L} = 0.014$; see also Table S3). This primarily has the effect of lowering the lift coefficient for minimum profile drag, and secondary, within the observed range for spanwise camber, to lower the minimum profile drag. The effect of primary separation is uncertain ($p_{\eta_p} = 0.16$; see also Table S3), but may be to increase profile drag.

The body drag coefficient decreases strongly with speed (-0.056 ± 0.002 per m s^{-1}) and there is a clear relation with glide angle (0.092 ± 0.003 per degree) (Fig. 10A). Theoretically we may expect the body drag to vary with the cube of the body angle (Hoerner, 1965): $\Delta C_{D_b} = \sqrt{4l_b^2/\pi S_b} C_{D_c} |\sin^3 \alpha_b|$. If we add this relation, with a body length estimate of $l_b = 0.3$ m and a cross-sectional drag coefficient $C_{D_c} = 1$, to a baseline $C_{D_b} = 0.2$ in Fig. 10B, it lines up with the lower values of body drag coefficient with respect to body angle. However, this pattern explains only little of the observed variation in body drag coefficient ($r^2 = 0.06$; see also Table S4). As tail profile drag is included in the measurement of body drag, we may expect the body drag coefficient to vary with tail area, as shown in Fig. 10C. If pressure drag is negligible (Thomas, 1993), the increase in body drag coefficient due to tail profile drag will be almost proportional to the tail area: $\Delta C_{D_{b,t}} = C_{D_{\text{pro,t}}} S'_t/S_b$. Including tail

area in the model, removes any significance of the body angle, and an estimated correlation coefficient with S'_t/S_b of 0.11 ± 0.01 is found ($r^2 = 0.58$; see also Table S5). However, this is roughly an order of magnitude more than expected for the friction drag coefficient $C_{D_f} = 2.66/\sqrt{Re_t}$, with Re_t the mean chord Reynolds number of the tail. This suggests tail pressure drag is not negligible. If we assume that the tail lift coefficient is proportional to the tail area, we would instead expect a cubic scaling with tail area: $\Delta C_{D_{b,t}} \propto (S'_t/S_b)^3$. This results in a coefficient of 0.0093 ± 0.0009 (see also Table S5). If we assume $C_{L_{t,max}} \approx 1$ corresponding to $(S'_t/S_b)_{max} \approx 3$, this would correspond to a value $k_{pro,t} \approx 0.08$ (i.e. $C_{D_{p,t}} = k_{pro,t}C_{L_t}^2$), which is reasonable for low aspect ratio wings at Reynolds numbers between 30×10^3 and 60×10^3 (Spedding and McArthur, 2010), such as the tail under consideration.

Discussion

Progress in quantitative wake analysis

In this study we computed induced drag, wing profile drag and body drag from the wake velocity measurements taken from a jackdaw gliding in a wind tunnel. For this we used a method for determining induced drag that is new to animal flight studies. Wake velocity data have been used to estimate aerodynamic forces in flying animals before, e.g. (Bomphrey, 2006; Henningsson and Hedenström, 2011; Muijres et al., 2011; Spedding, 1987), but in these studies simplified wake models were used. In an experiment with a kestrel (*Falco tinnunculus*) gliding through a cloud of helium filled soap bubbles the circulation in the trailing wing tip vortex could be estimated, from which the approximate lift force could be computed (Spedding, 1987). A similar approach for estimating lift was used in later studies. Body drag was measured using an approach similar to equation (11) for a common swift (*Apus apus*) by Henningsson and Hedenström (Henningsson and Hedenström, 2011). However, neither profile drag nor induced drag was measured, so they assumed a span efficiency and then subtracted (measured) body drag and (estimated) induced drag from the total drag to obtain wing profile drag. Recently, induced drag has been estimated in terms of the down-wash distribution in the wake using a form of lifting line model (Bomphrey et al., 2006; Henningsson et al., 2014; Muijres et al., 2011). However, these models rely on the assumption that the wake maintains the shape of the lifting line as it leaves the wing, an assumption that is violated by the rapid formation of trailing tip vortices. Instead equation (10) essentially measures the kinetic energy related to the trailing vorticity, a quantity that persists far downstream of the wing irrespective of wake deformation, making this the most robust approach for measuring induced drag.

Control of drag

All three drag components were involved in controlling the total drag. We related variation in the measured drag components to posture adjustments by the bird. Span reduction and the use of the tail appeared to be the primary variables affecting induced drag. Tail use also has considerable consequences for the body drag. The profile drag coefficient showed large variation, but we could only attribute a small portion of this variation to any of the measures of posture.

Induced drag

The separation of the outer primary feathers is often mentioned as an adaptation that improves the (shape specific) span efficiency (Berens, 2008; Cone, 1962; Eder et al., 2015; Kroo, 2001; Tucker, 1995). However, in our results we did not find such a relation. Also the degree of spanwise camber appeared not to have any noticeable effect on span efficiency. Instead, we could only relate the vertical gap between the tail and main wing to span efficiency, where it appears that using the tail has a negative effect on the span efficiency. This seems counterintuitive in the light of Prandtl's biplane model, which states that two vertically separated lifting surfaces can improve span efficiency (Thomas, 1996). This effect is described by the equation

$$\frac{1}{e'} = 1 - 2(1 - \sigma) \left(\frac{L_t}{W} \right) + \left(1 - 2\sigma + \left(\frac{b'_t}{b'_w} \right)^{-2} \right) \left(\frac{L_t}{W} \right)^2, \quad (14)$$

where the biplane coefficient σ decreases with increasing tail gap. For the jackdaw the tail to wingspan ratio $b'_t / b'_w < 0.3$ and the tail gap $\eta_t < 0.05$, corresponding to $\sigma > 0.8$. This means the tail can only improve span efficiency over the narrow range of tail loadings between 0 and 4% of the total weight. Outside this range the span efficiency rapidly decreases. This means that a larger tail gap itself will improve span

efficiency, but increased tail loading is accomplished by increasing angle of attack, thereby also increasing tail gap.

Considering that the use of the tail has a negative effect, the span efficiency is very close to unity; in fact for minimum tail deployment it is well above unity. As spanwise camber and primary separation were present across all tested conditions, these parameters are still likely to be involved in improving span efficiency, while the limited amount of variation prevents its detection. The span efficiencies we find for this jackdaw are generally much higher than those found for a common swift (Henningsson et al., 2014). As that study used a fundamentally different method, we cannot directly compare these values. However, it is worth noting that common swifts and jackdaws have comparable maximum lift to drag ratios at 12.5 (Henningsson and Hedenström, 2011) and 12.6 (Rosén and Hedenström, 2001), respectively, while the jackdaw has a higher body drag. Additionally, if we consider the Oswald efficiency factor, which combines the span efficiency with the lift dependent component of profile drag, expressed as $e_{\text{Oswald}} = \left(\frac{1}{e} + k_{\text{pro}} A \pi \right)^{-1}$, it follows that for large aspect ratio wings like those of common swifts ($A = b^2/S = 9.8$), there is less advantage for having a high span efficiency.

Profile drag

For the jackdaw we found profile drag coefficients with a magnitude of around 0.02, but with a rather large variation (s.d. = 0.005). A previous study measured profile drag of a Harris' hawk (*Parabuteo unicinctus*) using a wake rake to measure stagnation pressure (Pennycuick et al., 1992). They also found profile drag coefficients around 0.02, with a similar large scatter. It was noted that this could have been due to subtle adjustments of the hand wing near the wrist. We found some

support that wing shape, particularly the spanwise camber, may play a role in controlling the profile drag. However, the effect of spanwise camber could only explain a small portion of the observed variation (residual s.d. = 0.004). A detailed reconstruction of the wing surface around the wrist could possibly resolve this matter at some point. Another reason for large unexplained variation in profile drag could be due to ignoring tail lift. The profile drag coefficient of the main wing would be

$$C_{D_{\text{pro}}} = C_{D_0} + k_{\text{pro}} \left(\hat{C}_L \left(1 - \frac{L_t}{W} \right) - C'_{L_{D_{\text{pro,min}}}} \right)^2, \quad (15)$$

where $\hat{C}_L = W/qS_w'$. However, tail lift should be related to tail span or tail area, and neither seemed to be appreciably correlated to our measures of profile drag. Possibly the explanation for the large unexplained variation is simply that it represents measurement error. Both profile drag and body drag are calculated as the difference between two large quantities. For the wing profile drag this difference is particularly small, so that measurement error in the velocity field will have a relatively large influence. As a rough estimate we could use $\sigma_{C_{D_{\text{pro}}}} \approx (2S_{\text{pro}}/U_{\infty}S_w) \sigma_u$, which is derived from $\sigma_{C_{D_{\text{pro}}}}^2 = \sum \left(\frac{\partial}{\partial u_i} \frac{(u(u-U_{\infty})\Delta S_{\text{pro}})}{\frac{1}{2}\rho U_{\infty}^2 S_w} \right)^2 \sigma_{u_i}^2$, assuming that $\frac{u}{U_{\infty}} \ll 1$. With $S_{\text{pro}} \approx 0.015 \text{ m}^2$ the area of the wake over which equation (12) was evaluated and $\sigma_u \approx 0.1 \text{ m s}^{-1}$ the random uncertainty on the streamwise component of the measured velocity field. At 10 m s^{-1} this results in $\sigma_{C_{D_{\text{pro}}}} \approx 0.005$, which is of the same order of magnitude as the residual variation after taking into account the measures of posture.

Body drag

In previous studies widely varying values for body drag have been found. These were mostly based on mounted frozen bird bodies on a balance in a wind tunnel (e.g. Pennycuick, 1968; Pennycuick et al., 1988; Tucker, 1990). Body drag coefficients

varied roughly between 0.2 and 0.4. The validity of these wind tunnel measurements has been questioned (Tucker, 1990), both because of interference drag with the balance mount and possible imperfections in the preening of contour feathers. A smooth model of a peregrine falcon (*Falco peregrinus*) had 40% lower drag than the frozen body it represented, lowering the body drag coefficient to 0.15. Body drag coefficients as low as 0.05 have been proposed (Pennycuick et al., 1996). In a study measuring terminal velocity of small passerines body drag coefficients ranging from 0.17 to 0.77 were found (Hedenström and Liechti, 2001). However, these coefficients were based on the body frontal area relation for waterfowl and raptors: $S_b = 0.00813m^{0.666}$ (Pennycuick et al., 1988), whereas for passerines body frontal area is better represented by the relation $S_b = 0.0129m^{0.614}$ (Rosén et al., 2003), which makes the lowest estimated body drag coefficient 0.08 and the highest 0.39, with the majority of data points falling between 0.1 and 0.2. For swifts (*Apus apus*) a body drag coefficient was measured varying from 0.3 at the lowest speeds to 0.22 at high speeds, using the same method as in the current paper (Henningsson and Hedenström, 2011).

Several studies mentioned above found a negative relation between speed and body drag coefficient, in the case of mounted frozen bodies clearly independent of body angle or tail use. This was interpreted as a transition through flow regimes (characterized by Reynolds number; Pennycuick et al., 1988). At low Reynolds numbers the flow is less inclined to follow the shape of the body due to a laminar boundary layer, resulting in a large low-pressure area behind the body. In the transitional regime, higher Reynolds numbers promote the transition to turbulent boundary layers, which better resist flow separation. This effect may well have played a role for the jackdaw in the present study. However, the change in body drag

coefficient we measured was too dramatic (more than a factor 2) to be fully explained by this phenomenon. Because tail profile drag was included in our measurement of body drag, we think the strong correlation with tail area plays a more dominant role for the jackdaw. For a completely furled tail the body drag coefficient was around 0.2. Few studies have experimentally investigated the effect of the tail on body drag (Johansson and Hedenström, 2009; Maybury and Rayner, 2001). These focused on the function of the tail in folded condition to potentially act as a splitter plate reducing the large low-pressure region behind the body. Tail profile drag was included in a bird flight model aimed at studying the function of the avian tail, but only as flat plate skin friction (Thomas, 1993). However, this friction drag would account for an effect an order of magnitude less than what we observed. Our results indicate that the high body drag coefficient at low speeds is better explained by the pressure component of the tail profile drag.

Finally, it should be noted that bird feet can act as very efficient airbrakes, adding up to 20% to the body drag when lowered completely into the flow (Pennycuick, 1968). Regrettably we had no cameras recording the position of the feet, so we were not able to relate body drag coefficient to position of the feet. However, from direct observations it can be said that the legs of the jackdaw were extended to different degrees depending on the flight speed and at the highest flight speeds they were retracted close to the body. The feet were never tucked under the feathers.

Concluding remarks

Our results show that birds can control aerodynamic drag by using a variety of adjustments in posture. Notably the use of the tail appears to have a larger effect than often assumed in models used for estimating flight performance in birds, such as the program *Flight 1.25* (Pennycuick, 2008).

We also would like to stress the need for caution when using default values for coefficients suggested by said software, as for example the default body drag coefficient of 0.1 is half the minimum body drag coefficient we measured for this jackdaw.

List of symbols and abbreviations

b_w	Maximum wingspan
$b'_{<>}$	In-flight span of wings (b'_w) or tail (b'_t)
C_D	Drag coefficient $C_D = D/qS_w$
C'_D	Drag coefficient for specific in-flight wing area
C_L	Lift coefficient $C_L = L/qS_w$
C'_L	Lift coefficient for specific in-flight wing area
D	Drag force
e	Span efficiency
e'	Span efficiency for specific in-flight wing span
L	Lift force
q	Dynamic pressure $q = \frac{1}{2}\rho U_\infty^2$
Re	Reynolds number
S_b	Body frontal area
S_t	Tail area
S_w	Maximum wing area
S'_w	In-flight wing area
\mathbf{u}	Wake velocity vector field with components u , v , and w in the x , y and z directions respectively.
U_∞	Free-stream speed
W	Weight of the bird
β	Span ratio with maximum wingspan $\beta = b'_w/b_w$
γ	Glide angle

ζ	Area ratio $\zeta = S'_w / S_w$
η_p	Vertical separation of primary δ normalized to in-flight span
η_t	Vertical tail gap normalized to in-flight span
η_w	Spanwise camber normalized to in-flight span
ρ	Density
ψ	Stream function
ω	Streamwise component of the velocity field $\omega = (\nabla \times \mathbf{u}) \cdot \mathbf{i}$

Acknowledgements

We thank Johan Nilsson for providing us with the jackdaw. We are also grateful to the members of the Animal Flight Lab for their occasional assistance during the experiments and with taking care of the jackdaw.

Competing interests

We have no competing interests.

Author contributions

M.K. and A.H. conceived the study; M.K. and K.W. trained the bird and carried out the experiments; M.K. analysed the data. M.K. drafted the initial draft of manuscript. All authors contributed to the final manuscript.

Funding

The research received funding from the Knut and Alice Wallenberg foundation to A.H., from the Swedish Research Council to A.H. [621-2009-4965; 621-2012-3585], the Royal Physiographic Society in Lund to M.K..

References

- Barlow, J. B., Rae, W. H. and Pope, A.** (1999). *Low-speed wind tunnel testing*. 3rd ed. Wiley.
- Baudinette, R. V. and Schmidt-Nielsen, K.** (1974). Energy cost of gliding flight in herring gulls. *Nature* **248**, 83–84.
- Berens, M.** (2008). Potential of Multi-Winglet Systems to Improve Aircraft Performance.
- Bomphrey, R. J.** (2006). Insects in flight: direct visualization and flow measurements. *Bioinspir. Biomim.* **1**, S1–9.
- Bomphrey, R. J., Taylor, G. K., Lawson, N. J. and Thomas, A. L. R.** (2006). Digital particle image velocimetry measurements of the downwash distribution of a desert locust *Schistocerca gregaria*. *J. R. Soc. Interface* **3**, 311–7.
- Cone, C. D.** (1962). *NASA TR R-139 The Theory of Induced Lift and Minimum Induced Drag of Nonplanar Lifting Systems*.
- Van Dam, C. P.** (1999). Recent experience with different methods of drag prediction. *Prog. Aerosp. Sci.* **35**, 751–798.
- Van Dam, C. P., Nikfetrat, K. and Vijgen, P. M. H. W.** (1993). Lift and drag calculations for wings and tails: Techniques and applications. In *Fluid Dynamics in Biology* (ed. Cheer, A. Y. and Van Dam, C. P.), pp. 463–472. American Mathematical Society.
- Eder, H., Fiedler, W. and Neuhäuser, M.** (2015). Evaluation of aerodynamic parameters from infrared laser tracking of free-gliding white storks. *J. Ornithol.*
- Giles, M. B. and Cummings, R. M.** (1999). Wake Integration for Three-Dimensional Flowfield Computations: Theoretical Development. *J. Aircr.* **36**, 357–365.
- Hedenström, A.** (1993). Migration by Soaring or Flapping Flight in Birds: The Relative Importance of Energy Cost and Speed. *Philos. Trans. R. Soc. B Biol. Sci.* **342**, 353–361.
- Hedenström, A. and Liechti, F.** (2001). Field estimates of body drag coefficient on the basis of dives in passerine birds. *J. Exp. Biol.* **204**, 1167–75.
- Henningsson, P. and Hedenström, A.** (2011). Aerodynamics of gliding flight in common swifts. *J. Exp. Biol.* **214**, 382–93.
- Henningsson, P., Hedenström, A. and Bomphrey, R. J.** (2014). Efficiency of Lift Production in Flapping and Gliding Flight of Swifts. *PLoS One* **9**, e90170.
- Hoerner, S. F.** (1965). *Fluid-Dynamic Drag*. Hoerner Fluid Dynamics.

- Johansson, L. C. and Hedenström, A.** (2009). The vortex wake of blackcaps (*Sylvia atricapilla* L.) measured using high-speed digital particle image velocimetry (DPIV). *J. Exp. Biol.* **212**, 3365–3376.
- Kroo, I. M.** (2001). Drag due to lift: Concepts for Prediction. *Annu. Rev. Fluid Mech.* **33**, 587–617.
- Lentink, D., Müller, U. K., Stamhuis, E. J., de Kat, R., van Gestel, W., Veldhuis, L. L. M., Henningsson, P., Hedenström, A., Videler, J. J. and van Leeuwen, J. L.** (2007). How swifts control their glide performance with morphing wings. *Nature* **446**, 1082–5.
- Maybury, W. J. and Rayner, J. M. V.** (2001). The avian tail reduces body parasite drag by controlling flow separation and vortex shedding. *Proc. Biol. Sci.* **268**, 1405–10.
- Muijres, F. T., Spedding, G. R., Winter, Y. and Hedenström, A.** (2011). Actuator disk model and span efficiency of flapping flight in bats based on time-resolved PIV measurements. *Exp. Fluids* **51**, 511–525.
- Noca, F., Shiels, D. and Jeon, D.** (1999). A comparison of methods for evaluating time-dependent fluid dynamic forces on bodies, using only velocity fields and their derivatives. *J. Fluids Struct.* **13**, 551–578.
- Van Oudheusden, B. W., Scarano, F. and Casimiri, E. W. F.** (2006). Non-intrusive load characterization of an airfoil using PIV. *Exp. Fluids* **40**, 988–992.
- Pennycuik, C. J.** (1968). A wind-tunnel study of gliding flight in the pigeon *Columba livia*. *J. Exp. Biol.* **49**, 509–526.
- Pennycuik, C. J.** (1971). Gliding flight of the white-backed vulture *Gyps africanus*. *J. Exp. Biol.* **55**, 13–38.
- Pennycuik, C. J.** (2008). *Modelling the flying bird*. Amsterdam, The Netherlands: Elsevier.
- Pennycuik, C. J., Obrecht III, H. H. and Fuller, M. R.** (1988). Empirical estimates of body drag of large waterfowl and raptors. *J. Exp. Biol.* **135**, 253–264.
- Pennycuik, C. J., Heine, C. E., Kirkpatrick, S. J. and Fuller, M. R.** (1992). The profile drag of a hawk's wing, measured by wake sampling in a wind tunnel. *J. Exp. Biol.* **165**, 1–19.
- Pennycuik, C. J., Klaassen, M., Kvist, A. and Lindström, Å.** (1996). Wingbeat frequency and the body drag anomaly: wind-tunnel observations on a thrush nightingale (*Luscinia luscinia*) and a teal (*Anas crecca*). *J. Exp. Biol.* **199**, 2757–65.

- Pennycuik, C. J., Alerstam, T. and Hedenström, A.** (1997). A new low-turbulence wind tunnel for bird flight experiments at Lund University, Sweden. *J. Exp. Biol.* **200**, 1441–9.
- Rosén, M. and Hedenström, A.** (2001). Gliding flight in a jackdaw: a wind tunnel study. *J. Exp. Biol.* **204**, 1153–66.
- Rosén, M., Hedenström, A. and Rosén, M.** (2003). Body frontal area in passerine birds. *J. Avian Biol.* **34**, 159–162.
- Spedding, G. R.** (1987). The wake of a kestrel (*Falco tinnunculus*) in gliding flight. *J. Exp. Biol.* **127**, 45–57.
- Spedding, G. R. and McArthur, J.** (2010). Span Efficiencies of Wings at Low Reynolds Numbers. *J. Aircr.* **47**, 120–128.
- Spedding, G. R., Hedenström, A. and Rosén, M.** (2003). Quantitative studies of the wakes of freely flying birds in a low-turbulence wind tunnel. *Exp. Fluids* **34**, 291–303.
- Thomas, A. L. R.** (1993). On the Aerodynamics of Birds' Tails. *Philos. Trans. R. Soc. B Biol. Sci.* **340**, 361–380.
- Thomas, A. L. R.** (1996). Why do birds have tails? The tail as a drag reducing flap, and trim control. *J. Theor. Biol.* **183**, 247–253.
- Tucker, V. A.** (1987). Gliding birds: the effect of variable wing span. *J. Exp. Biol.* **133**, 33–58.
- Tucker, V. A.** (1990). Body drag, feather drag and interference drag of the mounting strut in a peregrine falcon, *Falco peregrinus*. *J. Exp. Biol.* **149**, 449–468.
- Tucker, V. A.** (1993). Gliding birds: reduction of induced drag by wing tip slots between the primary feathers. *J. Exp. Biol.* **180**, 285–310.
- Tucker, V. A.** (1995). Drag reduction by wing tip slots in a gliding Harris' hawk, *Parabuteo unicinctus*. *J. Exp. Biol.* **198**, 775–81.
- Tucker, V. A. and Heine, C. E.** (1990). Aerodynamics of gliding flight in a Harris' Hawk, *Parabuteo unicinctus*. *J. Exp. Biol.* **149**, 469–489.
- Tucker, V. A. and Parrott, G. C.** (1970). Aerodynamics of gliding flight in a falcon and other birds. *J. Exp. Biol.* **52**, 345–367.

Figures

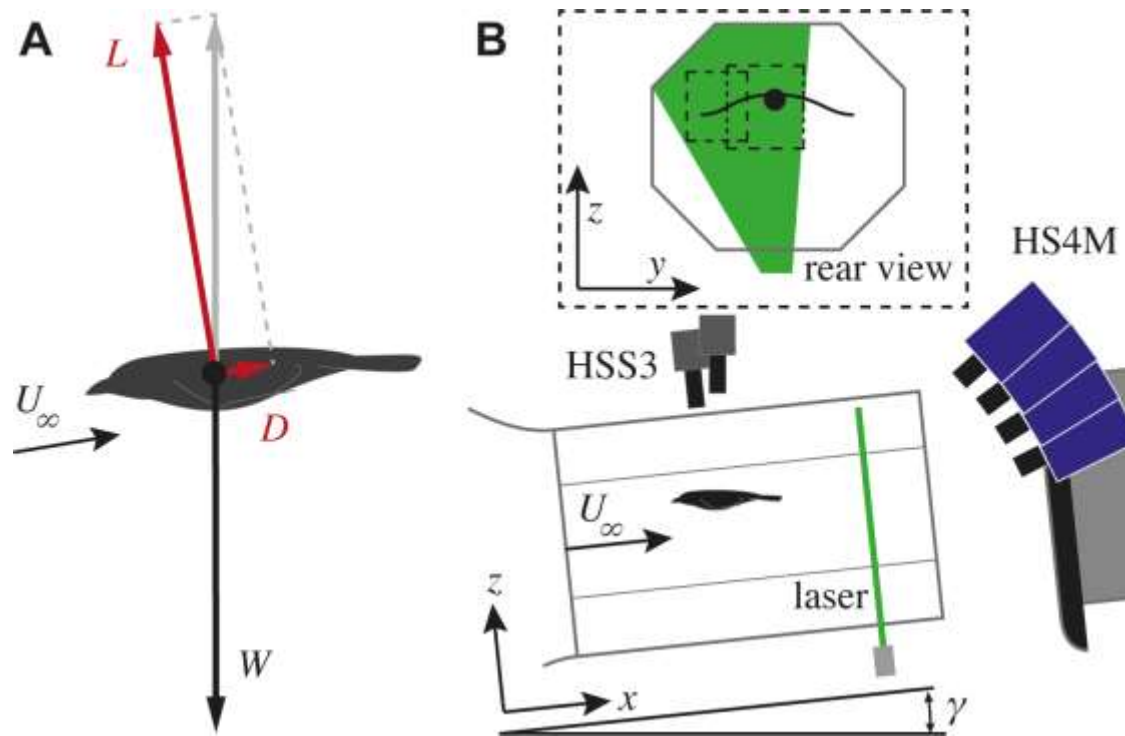


Fig. 1 Schematic representation of the wind tunnel setup for measuring glide performance. (A) Force balance on a bird in steady glide. The vector sum of lift L and drag D balance the weight W . (B) The wind tunnel is tilted to a glide angle $\gamma = \{4.5^\circ, 5.0^\circ, 5.5^\circ, 6.0^\circ\}$. Two high-speed cameras (HSS3) record the posture of the gliding bird. Four high-speed cameras (HS4M) record the movement of suspended oil droplets, which are illuminated by a laser sheet (laser). The inset (rear view) shows the two fields of view of the double stereo PIV configuration: one capturing the wake from the wing tip and the other capturing the wake from the central wing and body.

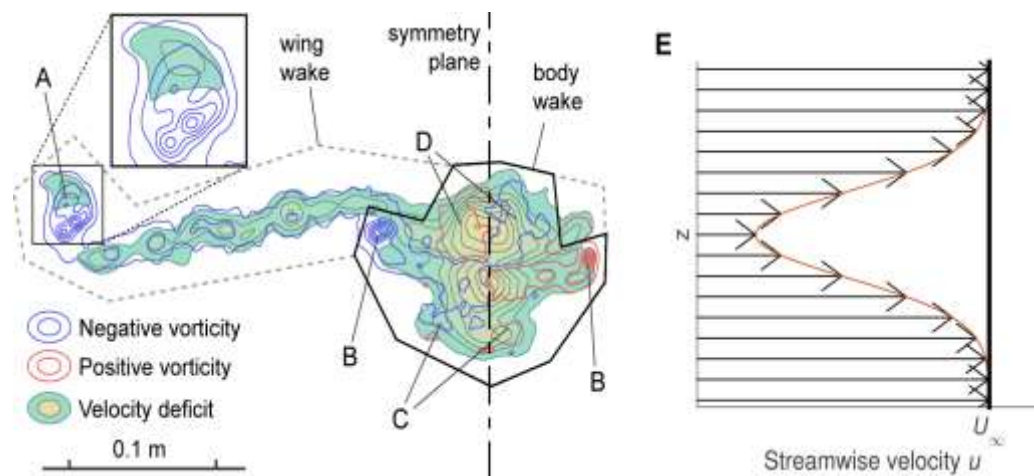


Fig. 2 Visualisation of wake vorticity and velocity deficit at 7.6 m s^{-1} . (A) Wing tip vortex, showing multiple vortex cores. Vorticity shed along the entire wingspan. (B) Tail tip vortex. Vorticity is found along the entire span of the tail. The tail is contributing positive lift. (C) Lower vortex pair of body quadrupole of lower strength and than upper vortex pair (D). Filled contours indicate streamwise velocity deficit. Also indicated are the symmetry plane, the selected region enclosing the body drag and that enclosing the wing profile drag. (E) Schematic representation of the velocity deficit, observed as a vertical slice through the measurement plane. The thick line indicates the free stream velocity.

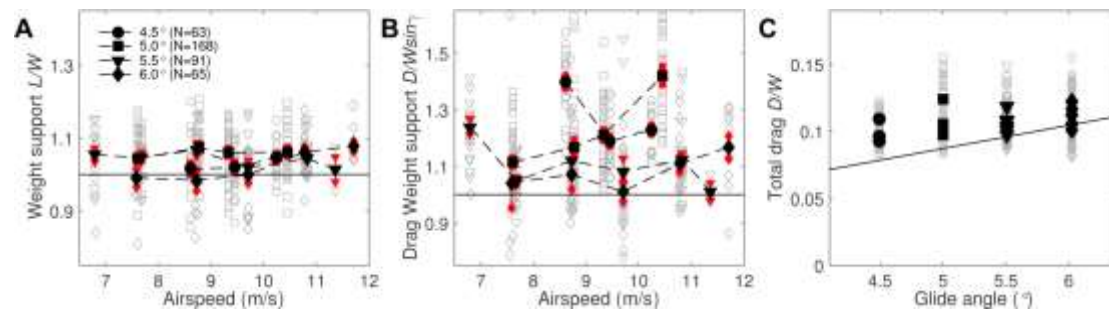


Fig. 3 Weight support and drag weight support for the different combinations of glide angle and airspeed. Grey markers indicate raw data points. Black closed markers indicate means within groups of 1 m/s bins and 1 degree bins for glide angles, with the smaller (red) filled markers indicating the corresponding standard errors. This will be used across for all plots following. Broken lines connect the means within glide angle group. (A) Average total weight support is close to one. Solid line indicates proper weight support. (B) Average drag weight support increases with reducing tilt angles. Solid line indicates proper weight support. (C) Total drag over weight ($D/W = \sin \gamma$) against the wind tunnel tilt angle. Solid line indicates proper weight support.

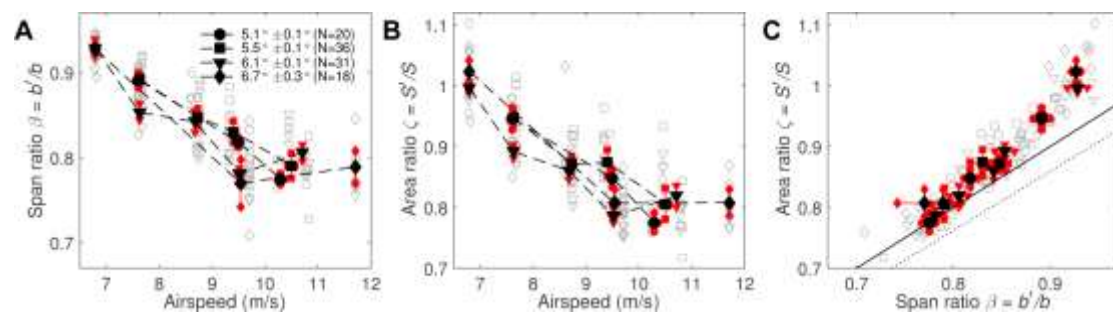


Fig. 4 Wingspan and wing area decrease with speed and are approximately proportional to each other. See legend Fig. 3. (A) Wing span ratio as a function of speed averaged for binned equivalent glide angles. (B) Wing area ratio against speed. (C) Wing area ratio against wing span ratio. Solid line indicates 1:1 relation. Dotted line indicates regression from (Rosén and Hedenström, 2001).

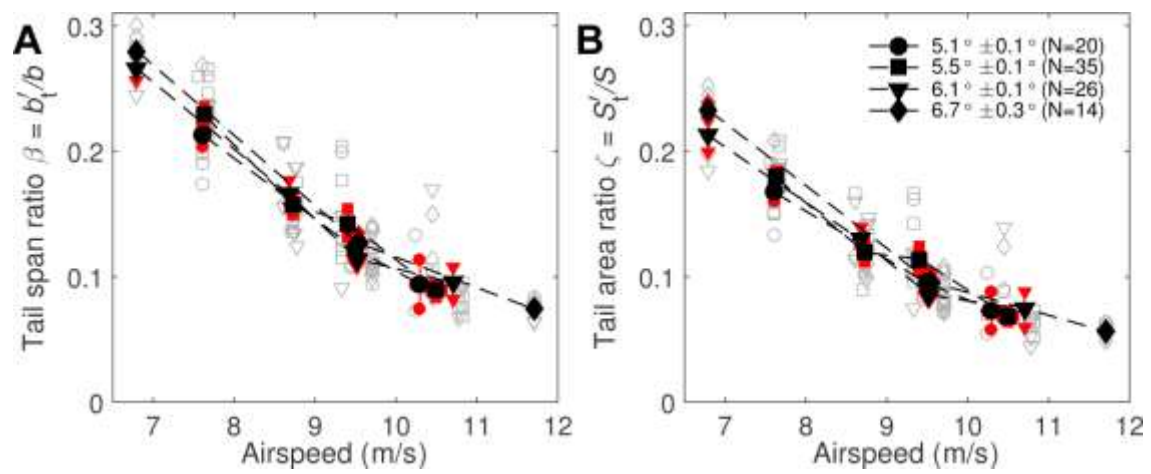


Fig. 5 Tail span and tail area decreases with speed. See legend Fig. 3. (A) Tail span relative to the maximum wingspan. Maximum tail span is just over 25% of the maximum wingspan while the minimum is around 10%. (B) Tail area relative to maximum wing area. Maximum tail area is just over 20% of the maximum wing area.

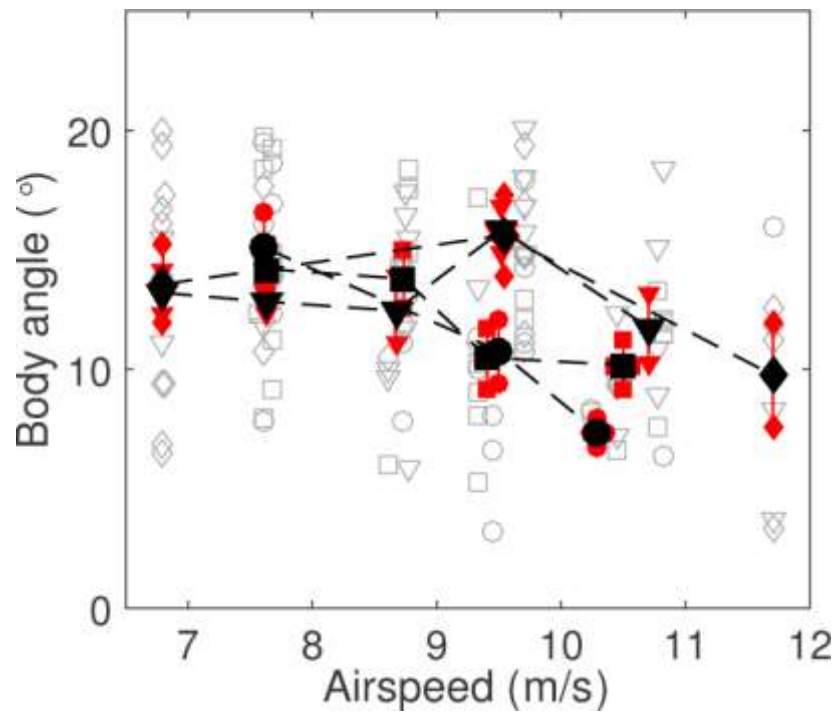


Fig. 6 Body angle for different combinations of glide angle and airspeed. See legend Fig. 3. Body angle, measured as the angle between the line from the neck (point 27) to the rump (point 28).

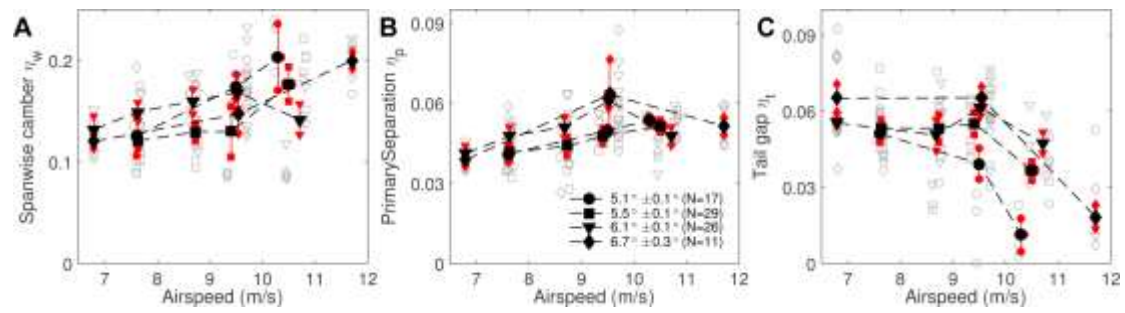


Fig. 7 Measures of non-planar features for different combinations of equivalent glide angle and airspeed. See legend Fig. 3. (A) Spanwise camber, the relative height of the circle arc segment fitted through the trailing edge feathers. (B) Primary separation (primary 8), the distance away from the fitted circle arc segment. (C) Vertical tail gap between the trailing edge of the tail and that of the secondary feathers.

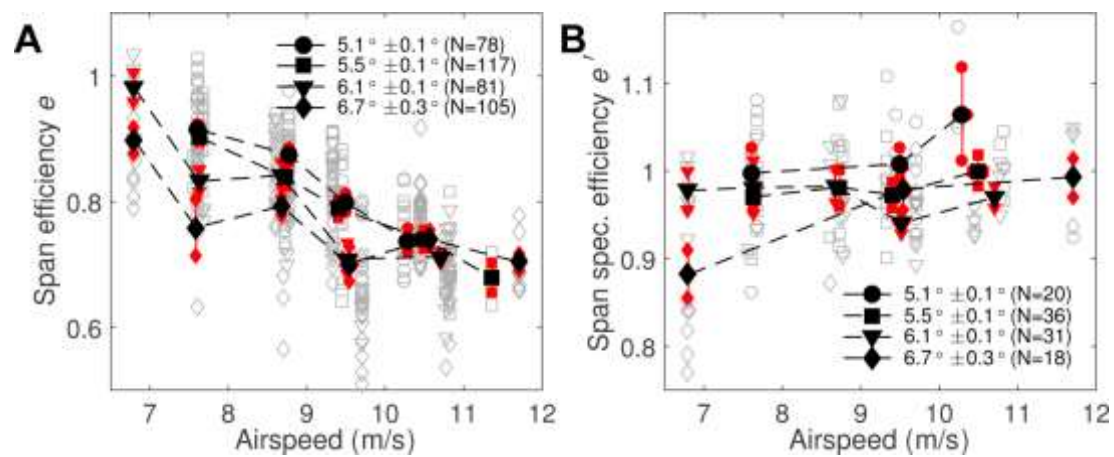


Fig. 8 Variation in span efficiency. See legend Fig. 3. (A) Span efficiency using maximum wingspan in shows a clear decrease with speed. (B) Span efficiency specific for the in-flight wingspan has much less variation (note vertical axis scale from 0.8 to 1.1)

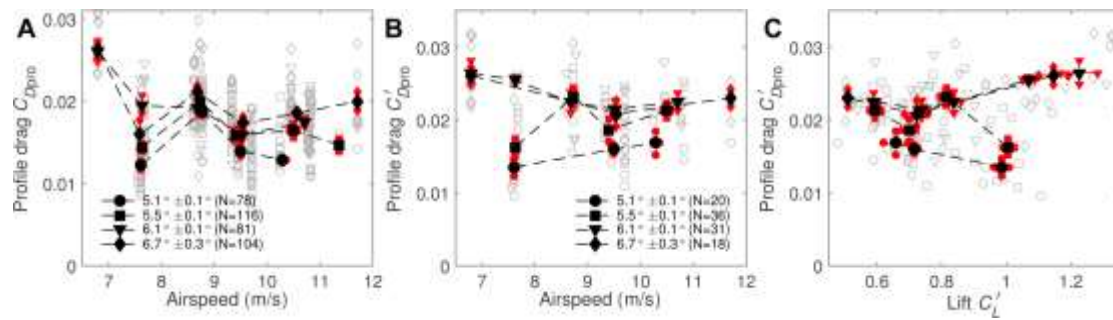


Fig. 9 Variation in the wing profile drag coefficient. See legend Fig. 3. (A) Profile drag coefficient relative to maximum wing area as a function of speed. (B) Shape-specific profile drag coefficient (relative to in-flight wing area) as a function speed. Primarily the right hand side of the graph is raised compared to (A) due to the decreased wing area at higher speeds. (C) Shape-specific profile drag coefficient against shape-specific lift coefficient (both based on in-flight wing area). The lower bound, corresponding to the lowest equivalent glide angle, appear to decrease with increasing lift coefficient.

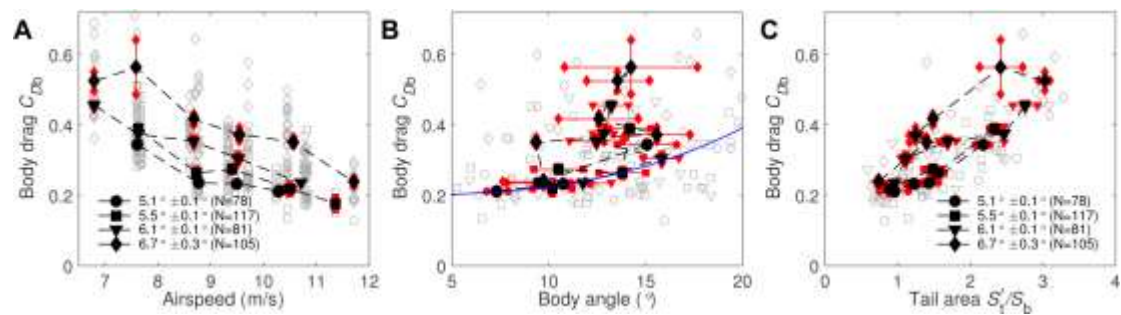


Fig. 10 Variation in the body drag coefficient. See legend Fig. 3. (A) Body drag coefficient decreases with speed and is distinctly lower for steeper equivalent glide angles. (B) With respect to body angle the lower bound of group-averaged body drag coefficients appears to line up with a rough estimate based on an inclined cylinder. Around 15° body angle the body drag coefficients diverge upward away from this relation (encircled markers). (C) Body drag coefficient increases strongly with increasing tail area, indicating influence of tail profile drag.